



# Numerical investigation of roughness effect on wet steam ejector performance in the refrigeration cycle

Mehdi Pouyan Rad<sup>1</sup> · Esmail Lakzian<sup>1,2</sup> · Aki Grönman<sup>3</sup>

Received: 2 August 2021 / Accepted: 1 March 2022

© The Author(s), under exclusive licence to Springer-Verlag GmbH Germany, part of Springer Nature 2022

## Abstract

Machining operation and presence of water droplets cause increase the surface roughness of wet steam ejector walls and change its performance in the refrigeration cycle. The purpose of this work is to investigate the influences of the primary nozzle surface roughness on wet steam ejectors in the refrigeration cycle with steam water as a working flow. The Eulerian-Eulerian model is validated by a comparison of numerical results with experimental data. Moreover, different surface roughness has been successfully applied to the primary nozzle, and its effect on the entire flow is shown. Six properties of wet steam are selected, including pressure, temperature, Mach number, average droplet radius, droplet growth rate, and liquid mass fraction. The result shows increasing roughness resulted in a shift of the shock chain to the primary nozzle, damping shock strength, and rising temperature in the diffuser. In addition, increment of the primary nozzle surface roughness decreases ER and COP of the refrigeration cycle by 3.67% and 3.8%, respectively. The designers and operators should be considered the roughness effects in the design and operation of wet steam ejectors due to the vital impact of the roughness on the liquid mass fraction, average droplet radius, droplet growth rate, ER, and COP.

## Nomenclature

|               |  |            |  |
|---------------|--|------------|--|
| $D_\omega$    | Cross-diffusion term ( $\text{kgm}^{-1} \text{s}^{-3}$ )                 | $\dot{m}$  | Mass flow rate ( $\text{kg s}^{-1}$ )                        |
| E             | Total energy (J)   | Ma         | Mach number  |
| ER            | Entrainment ratio (-)  | P          | Pressure (Pa)  |
| $f_r$         | Roughness function (-)   | $\dot{Q}$  | Rate of heat exchange ( $\text{W m}^{-2} \text{s}^{-1}$ )    |
| G             | Gibbs free energy ( $\text{J kg}^{-1}$ )                                 | $q_c$      | Condensation coefficient (-)                                 |
| $\tilde{G}_k$ | Turbulence kinetic energy generation ( $\text{kgm}^{-1} \text{s}^{-3}$ ) | $r_*$      | Critical radius of droplets ( $\mu\text{m}$ )                |
| $G_\omega$    | Generation of $\omega$ ( $\text{kgm}^{-1} \text{s}^{-3}$ )               | r          | Droplet radius ( $\mu\text{m}$ )                             |
| h             | Enthalpy ( $\text{J kg}^{-1}$ )  | $\dot{r}$  | Droplet growth rate ( $\mu\text{m s}^{-1}$ )                 |
| J             | Nucleation rate ( $\text{m}^{-3} \text{s}^{-1}$ )                        | R          | Gas constant ( $\text{JK}^{-1} \text{mol}^{-1}$ )            |
| k             | Turbulent dissipation rate ( $\text{m}^2 \text{s}^{-3}$ )                | S          | Saturation ratio (-)   |
| $K_s^+$       | Non-dimensional roughness height   | $S_k$      | Source terms of $\omega$ ( $\text{kgm}^{-1} \text{s}^{-3}$ ) |
| $k_s$         | Physical roughness height (m)  | $S_\omega$ | Source terms of $\omega$ ( $\text{kgm}^{-1} \text{s}^{-3}$ ) |
| $K_B$         | Boltzmann's constant   | T          | Temperature (K)  |
| L             | Nozzle length(m)   | u          | Velocity ( $\text{m s}^{-1}$ )                               |
| m             | Mass of one molecule (mg)  | $V_d$      | Mean volume of the droplets ( $\text{m}^3$ )                 |
|               |  | x          | Spatial component (m)  |
|               |  | $Y_k$      | Dissipation of k ( $\text{kgm}^{-1} \text{s}^{-3}$ )         |
|               |  | $Y_\omega$ | Dissipation of $\omega$ ( $\text{kgm}^{-1} \text{s}^{-3}$ )  |

✉ Esmail Lakzian  
e.lakzian@hsu.ac.ir

<sup>1</sup> Center of Computational Energy, Department of Mechanical Engineering, Hakim Sabzevari University, Sabzevar, Iran

<sup>2</sup> Peoples' Friendship University of Russia (RUDN University), 6 Miklukho-Maklaya Street, 117198 Moscow, Russian Federation, Russia

<sup>3</sup> School of Energy Systems, LUT University, Yliopistonkatu 34, P.O. Box 20, 53851 Lappeenranta, Finland

## Greek symbols

|               |   |
|---------------|---|
| $\alpha$      | Thermal conductivity ( $\text{W m}^{-1} \text{K}^{-1}$ )  |
| $\beta$       | Liquid mass fraction (-)                                  |
| $\Gamma$      | Mass generation rate ( $\text{kg m}^{-3} \text{s}^{-1}$ ) |
| $\delta_{ij}$ | Rate of mixing layer growth (-)                           |
| $\eta$        | Number of droplets ( $\text{m}^{-3}$ )                    |
| $\mu$         | Dynamic viscosity (Pa s)                                  |
| $\rho$        | Density ( $\text{kg m}^{-3}$ )                            |

|                 |   |
|-----------------|---|
| $\sigma$        | Liquid surface tension ( $\text{N m}^{-1}$ )        |
| $\sigma_k$      | Indicate turbulent Prandtl numbers for $k$          |
| $\sigma_\omega$ | Turbulent Prandtl numbers for $\omega$              |
| $\tau$          | Stress tensor (Pa)                                  |
| $\omega$        | Specific turbulence dissipation ( $\text{s}^{-1}$ ) |

### Subscribes

|     |             |
|-----|-------------|
| s   | Secondary   |
| p   | Primary     |
| e   | Exit        |
| g   | Gas (vapor) |
| eff | Effective   |
| l   | Liquid      |
| v   | Vapor       |

### Abbreviation

|     |                     |
|-----|---------------------|
| CAE | Constant Area Exit  |
| MCE | Mixing Chamber Exit |
| PNE | Primary Nozzle Exit |

### Math symbols

|   |         |
|---|---------|
| - | Average |
|---|---------|

## 1 Introduction

A wide range of applications, simple structure, energy-saving, and reducing environmental pollution has made ejectors attractive equipment for researchers as well as industrial equipment manufacturers. Vast numerical and experimental studies performed in recent decades can help the manufacturers of this equipment to upgrade their products for future systems. In addition to machining operation, high pressure and velocity and sometimes corrosive gases and liquids cause corrosion/erosion of the ejector surfaces, which means increasing the surface roughness and changing in ejector performance during operation. Corrosion/erosion may be more evident in wet steam ejectors due to the presence of high-speed condensed droplets that hit the inner surface of the ejector and makes it rough. Therefore, surface roughness can play a significant role in the operation of ejectors.

Various experimental and numerical studies have been published in the field of wet steam in nozzles and blades. The Eulerian-Eulerian approach with two methods of density-based and pressure-based can be used for modeling wet steam flow in fluent. Both methods have good similarities against experimental data [1]. Yazdani and Lakzian [2] applied the Eulerian-Lagrangian model to show the effect of impressing holes in the pressure and suction side of the blade on the performance of the steam turbine. They presented complete elimination of wetness when the inlet of holes is closer to the leading edge of the pressure and suction side. Condensed droplets in wet steam can be considered monodispersed or polydispersed models. These two models have been simulated

in a recent paper by Ding et al. [3] using exergy analysis and polydispersed model that shows more accurate results than the monodispersed model. In both mono and polydispersed model, two-phase flow can be considered as single-fluid or two-fluid, but two-fluid model can predict thermodynamic loss and indicates better agreement in droplet radius and drag forces with experimental data [4]. Particle Image Velocimetry (PIV) method was applied to investigate polydispersed condensing flow [5]. In a different method, impulse facility techniques with the aid of image post-processing tools can show several phenomena that occurred in nozzles. Among them, shock waves and condensation can be seen easily [6]. As mentioned previously, wet steam studies can be extended to more complex but similar geometries of the ejectors.

Although the focus of this study is on wet steam, in the general view, various fluids are used in ejectors based on their application including, water, air and, refrigerants. In refrigeration application, a comparison between 10 different fluids for ejector chillers shows that water has good performance but, the assumption of steam as ideal gas is not appropriate in the simulation of flow in wet steam ejector [7]. Besagni et al. [8] performed a numerical-based study on various working fluid and ejector geometry. They also investigated the effect of geometry on COP and temperature of the critical point of ejector operating curve. They divided refrigerants into three groups with high COP (0.5–1) and low critical temperature of (20.7–25.0 °C), intermediate COP (0.27–0.83) and critical temperature of (22.8–28.0 °C) and, low COP (0.25–0.58) and critical temperature of (26.0–31.0 °C). Perez et al. [9] studied the CO<sub>2</sub> ejector-expansion refrigeration cycle thermoeconomically. They increased COP by about 5.5% and reduced energy consumption.

Condensation creates a two-phase flow that wet steam solution gives more accurate results and improves the performance parameters of ejectors [10]. In addition to condensation that prevalently occurs in the primary nozzle, the results obtained by Faghieh et al. [11] indicated that the existence of droplet in motive flow postpones condensing shock and reduce motive and suction mass flow as well as entrainment ratio (ER). Furthermore, it is observed that reduction in the wetness of suction flow can increase ER and system performance [12]. In another work, a modified nucleation model by Zhang et al. [13] predicted a reduction in ER in the critical zone and increasing in critical zone length. On the other hand, reduction or elimination of condensation can help to the improvement of ejector performance. It has been proved that an increase in the degree of superheat in the primary inlet causes a delay in the location of nucleation and reduction of the intensity of the condensation shock [14] and increment of ER [15]. Yang et al. [16] investigated the effect of the area ratio of the primary nozzle on steam ejector performance. They indicated that the area ratio of 8 can increase the entrainment ratio to 0.75. Nucleation is one of

the main factors in the growth of the mixing layer between the primary and secondary flow. Ariafar et al. [17] argued that under a fixed condition for the primary and discharge, the mixing layer has maximum effect on ER at lower secondary pressure.

Similar to other scientific researches, experimental data were used as the main reference for validating the results in the ejectors. Obtained data by modern technic and advanced instruments on ejectors as well as convergent-divergent nozzles reveal several unseen phenomena that can conduct theoretical research into true path. Tang et al. [18] represented results of experimental setup that show the ununiformed distribution of droplets in each cross-section and increase of condensate quantity with entrainment ratio. In addition, Rayleigh scattering of the supersonic condensing jet flow and reverse condensing flows are photographed, and observed phenomena are discussed. In another experimental study, the result showed the starting main shock waves in critical pressure condition occurs between the mixing chamber and fixed area section [19].

In addition to the two-phase behavior of flow, one of the other parameters that researchers have addressed is the geometry of the ejector. Entropy generation, ER, critical compression ratio, and COP of refrigeration system are used by Foroozesh et al. [20] to modify the geometry of the ejector. They previously investigated the effect of the geometry of ejector on the performance of refrigeration systems based on entrainment ratio and critical compression ratio [21]. Lakzian et al. [22] optimized air ejector for carpet industrial and introduced optimal converging angle of the mixing chamber, length of the mixing chamber, the diameter of the primary nozzle, and outlet diameter of the diffuser. The new design improves ER and critical compression ratio by 32%. Dong et al. [23] examined the effect of the mixing chamber on performance, considering the deferent Mach number at the exit of the primary nozzle and length of the fixed area section and diffuser. Zhang et al. [24] reported that Genetic algorithm optimization of the primary nozzle geometry using modified nucleation model based Benson surface tension increases the ER of ejector approximately 27%. Zhang et al. [25] performed an analysis of four important parameter in ejectors, including latent heat, ejector performance, entrainment ratio, and different superheating degrees. They showed a higher degree of superheat causes a higher entrainment ratio, better performance, and lower two-phase latent heat.

Some other researchers have addressed the issue of surface roughness. Increasing the area ratio between the primary nozzle exit and throat reduces nozzle outlet pressure and condensation intensity and increases liquid mass fraction. Besides, an increase in surface roughness causes a reduction in mass flow rate and increases in dryness [26]. Mahmoudian et al. [27] tested a prototype ejector chiller

with R134a working refrigerant and briefly mentioned that the ejector with a smooth surface has higher performance. Energy loss is directly related to surface roughness in each part of ejectors with ideal gas as a working flow, but among them, diffuser surface roughness has a maximum impact [28]. Roughness values from  $5\mu$  to  $300\mu$  were investigated for the inner surface of the ejector by Zhang et al. [29]. Their results showed an increase in temperature and a reduction in the performance of the ejector. Arison and Brezgin [30] have presented similar results on ejector performance and pressure. Wang et al. [30] took into account friction on the throat, using the modified law of the wall, and indicated a reduction of entrainment of the ejector due to an increase in roughness. In fact, roughness acts like reverse pressure and displaces the shock waves upstream [31].

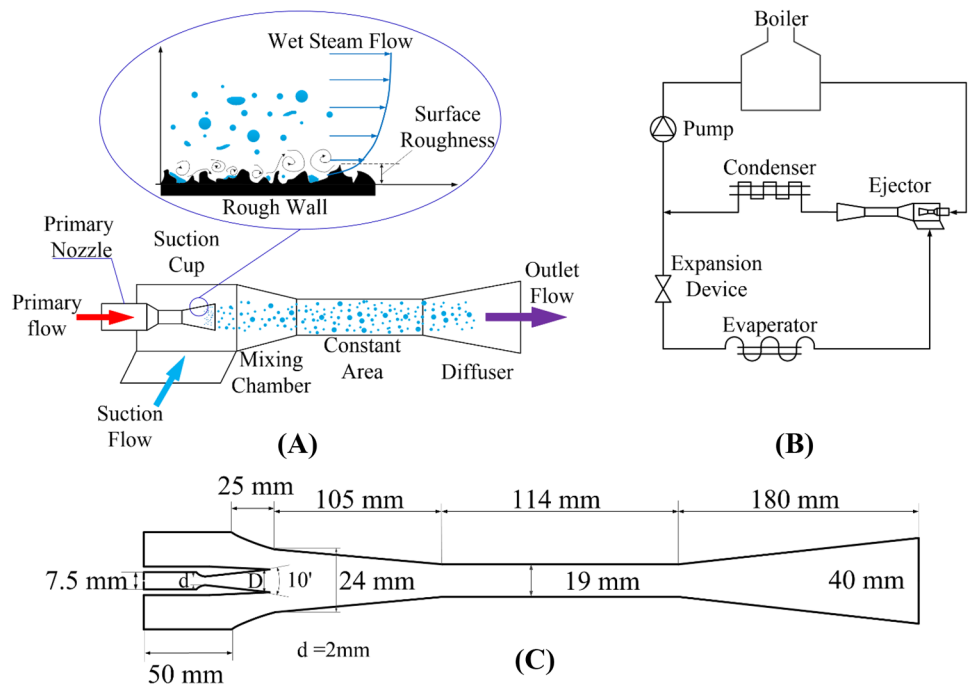
Researches demonstrate similar results in the investigation of roughness in blades and nozzles. In the study of the Laval nozzle, Pillai and Prasad [32] indicated that condensation shock strength is adjusted due to increasing roughness, but the thickness of the boundary layer increases. Han et al. [33] argued that an increase in surface roughness decreases Mach number and peak of nucleation rate in the turbine blade. In addition, Ding et al. [34] have demonstrated that an increase in average height of sand-grain roughness causes entropy generation growth. Investigations show more performance loss in the subsonic region compared to supersonic in turbine blades [35].

Even though several studies in the literature have been performed on the subject of roughness in ejectors, no researchers have addressed the effect of surface roughness on the ejector flow with water steam as a working fluid in the refrigeration cycle. Accordingly, the novelty of this work is a comprehensive investigation of the effect of the primary nozzle surface roughness on thermodynamic properties in ejectors, which can extend the information about ejector performance. These results are presented for the first time in the field of wet flow with water steam as a working fluid for refrigeration applications.

## 2 Problem definition

Figure 1A shows the schematic diagram of the studied ejector with rough walls. For a better understanding of the issue, a simple schematic of wall roughness has been magnified in this figure. The ejector consists of the primary nozzle, suction cup, mixing chamber, constant area, and diffuser. Water steam is expanded in the primary nozzle and causes a sharp drop in temperature and pressure. Under certain condition, the steam passes through the saturation line and rapidly enter the two-phase region. In this condition, steam is non-equilibrium and expands continually up to Wilson Line, where in terms

**Fig. 1** Schematic of (A) wet steam ejector and surface roughness in the primary nozzle, (B) water refrigeration cycle, and (C) dimensions of the ejector



of thermodynamic, the steam is super-cooled. Increase in the degree of supercooling and in the absence of external surfaces, the homogeneous nucleation occurs. This phenomenon is known as condensation shock.

Steam expansion continues in the mixing chamber, which is caused the pressure drops to approximately one-fifth of secondary pressure. Therefore, the secondary flow is sucked into the ejector. These two streams are mixed and then enter the constant area. From the outlet of the primary nozzle to the beginning of the diffuser, the pressure fluctuates and forms the shock chain. Then, it increases gradually to the outlet of the ejector. In the present study, wet steam flow in the ejector with different primary nozzle surface roughness is numerically analyzed. The ejector of the refrigeration cycle developed by Ruangtrakoon et al. [36] was selected as a case study (Fig. 1B). The total temperature at the primary, suction, and outlet flow of the ejector are 403 K, 283 K, and 300 K and total pressure for the same flow are 270 kPa, 1.228 kPa, and 4 kPa, respectively. Note that it is assumed the inner surface of the wall ejector is adiabatic.

The performance of the ejectors in the refrigeration cycle can be indicated by two key parameters of ER and COP as follows [20]:

$$ER = \frac{\dot{m}_s}{\dot{m}_p} \quad (1)$$

$$COP = \frac{\dot{Q}_{evap}}{\dot{Q}_{boiler}} = \frac{\dot{m}_s(h_{g(T_{evap})} - h_{f(T_{cond})})}{\dot{m}_p(h_{g(T_{boiler})} - h_{g(T_{evap})})} = ER \frac{\Delta h_{evap}}{\Delta h_{boiler}} \quad (2)$$

### 3 Mathematical modeling

#### 3.1 Governing equations

The steady-state compressible Navier–Stokes equations use for mixture flow, including continuum, momentum, and energy equation. These three equations can be simplified and written as follows:

$$\frac{\partial}{\partial x_i}(\rho u_i) = 0 \quad (3)$$

$$\frac{\partial}{\partial x_j}(\rho u_i u_j) = -\frac{\partial P}{\partial x_i} + \frac{\partial \tau_{ij}}{\partial x_j} \quad (4)$$

$$\frac{\partial}{\partial x_i}(u_i(\rho E + P)) = \frac{\partial}{\partial x_i}(\alpha_{eff} \frac{\partial T}{\partial x_i}) + \frac{\partial}{\partial x_i}(u_i \tau_{ij}) \quad (5)$$

where,  $\rho$ ,  $u$ ,  $P$ ,  $E$ ,  $T$ , and  $\alpha_{eff}$  are mixture density, velocity, pressure, total energy, temperature, and thermal conductivity, respectively [5].  $\tau_{ij}$  is viscous shear stress tensor and expressed as follows:

$$\tau_{ij} = \mu_{eff} \left( \frac{\partial u_i}{\partial x_j} + \frac{\partial u_j}{\partial x_i} \right) - \frac{2}{3} \mu_{eff} \frac{\partial u_k}{\partial x_k} \delta_{ij} \quad (6)$$

where  $\mu_{eff}$  and  $\delta_{ij}$  are dynamic viscosity and mixture layer growth rate. The virial third-order state equation that describes the relation of pressure, temperature, and vapor density ( $\rho_v$ ) is as follows:

$$P = \rho_v RT(1 + B\rho_v + C\rho_v^2) \quad (7)$$

where B and C are coefficients and can be found in thermodynamic references. Density of vapor  $\rho_v$  in state equation can be related to the density of mixture  $\rho$  in Navier–Stokes equations as follows:

$$\rho = \frac{\rho_v}{(1 - \beta)} \quad (8)$$

where  $\beta$  denotes liquid mass fraction. Some basic assumptions for modeling wet steam are as follows [37]:

- Vapor is the continuous phase.
- The droplets are spherical-shaped.
- There is zero relative velocity between vapor and liquid phases.
- Liquid phase volume and interaction between droplets are negligible.
- Liquid mass fraction is 0.2 or less.
- The minimum temperature of flow in this problem is 273.15 K.

Modeling non-equilibrium condensation needs two additional transport equations. These equations are transporting equation of liquid mass fraction (Eq. (9)) and number density of droplet (Eq. (10)) and can be defined as below [13]:

$$\frac{\partial(\rho\beta)}{\partial t} + \frac{\partial}{\partial x_i}(\rho u_i \beta) = \Gamma \quad (9)$$

$$\frac{\partial\rho\eta}{\partial t} + \frac{\partial}{\partial x_i}(\rho u_i \eta) = \rho J \quad (10)$$

where  $\Gamma$  is the rate of liquid mass generation due to exchanging between liquid and vapor phase and  $J$  is droplet nucleation rate per unit volume.  $\eta$  shows the number of droplets per unit volume. The following relation is used for the calculation of these three parameters:

$$\Gamma = \frac{3}{4}\pi\rho_l I r_*^3 + 4\pi\rho_l \eta \bar{r}^2 \frac{\partial \bar{r}}{\partial t} \quad (11)$$

$$J = \frac{q_c}{1 + \theta} \left(\frac{\rho_v^2}{\rho_l}\right) \sqrt{\frac{2\sigma}{M_m^3 \pi}} \exp\left(-\frac{4\pi r_*^2 \sigma}{3k_B T}\right) \quad (12)$$

$$\eta = \frac{\beta}{(1 - \beta)V_d\left(\frac{\rho_l}{\rho_v}\right)} \quad (13)$$

The function  $r_*$  is critical droplet radius that derived from Gibbs free energy equation under the condition of the stability of the droplet:

$$r_* = \frac{2\sigma}{\rho_l RT_v \ln Sr} \quad (14)$$

where  $\sigma$  is liquid surface tension at T and  $\rho_l$  is density of the condensed liquid.  $\frac{\partial \bar{r}}{\partial t}$  denotes the rate of droplet volume change due to the growth of existing droplets:

$$\frac{\partial \bar{r}}{\partial t} = \frac{p}{h_{lv}\rho_l \sqrt{2\pi RT}} \frac{C_p + C_v}{2} (T_s(p_v) - T_v) \quad (15)$$

where  $[T_s(p_v) - T_v]$  denotes degree of supercooling and  $\theta$  is Kantrowitz non-isothermal correction which is calculated as follows:

$$\theta = 2 \frac{\gamma - 1}{\gamma + 1} \frac{h_{lv}}{RT_v} \left(\frac{h_{lv}}{RT_v} - \frac{1}{2}\right) \quad (16)$$

By the assumption of the spherical form of droplets, the mean volume of the droplets is defined as:

$$V_d = \frac{4}{3}\pi \bar{r}^3 \quad (17)$$

### 3.2 Law-of-the-wall modified for roughness

Equation (18) shows the logarithmic profile of mean velocity used to take into account of surface roughness effect [26, 28, 32, and 39]:

$$\frac{u_p u^*}{\tau_w / \rho} = \frac{1}{\kappa} \ln\left(\frac{\rho u^* y_p}{\mu}\right) - \Delta B \quad (18)$$

where  $u_p$  is the velocity at the cell near the wall and  $u^*$  the wall friction velocity which can be defined as:

$$u^* = C_\mu^{1/4} k^{1/2} \quad (19)$$

$$\Delta B = \frac{1}{\kappa} \ln(f_r) \quad (20)$$

$$K_s^+ = \rho k_s u^* / \mu \quad (21)$$

$$\Delta B = \begin{cases} 0 & K_s^+ \leq 2.25 \\ \frac{1}{\kappa} \ln\left[\frac{K_s^+ - 2.25}{87.75} + C_s K_s^+\right] \times \sin[0.4258(\ln K_s^+ - 0.811)] & 2.25 \leq K_s^+ \leq 90 \\ \frac{1}{\kappa} \ln(1 + K_s^+) & K_s^+ \geq 90 \end{cases} \quad (22)$$

where  $f_r$ ,  $K_s^+$ ,  $k_s$ , and  $C_s$  are roughness function, nondimensional roughness height, physical roughness height, and roughness constant, respectively. Moreover,  $\Delta B$  depends on the type and size of the wall roughness that shows three equations for hydro-dynamically smooth, transitional, and fully rough surface.

### 3.3 Turbulent model

The  $SSTk - \omega$  turbulent model is selected in the present work. The SST  $k - \omega$  turbulence model is good to capture the condensation shock in high speed compressible wet steam flow in ejector. Furthermore, this model has good agreement with experimental data [38] and predicts shocks. This model can be expressed by the following equations:

$$\frac{\partial(\rho k)}{\partial t} + \frac{\partial(\rho k u_i)}{\partial x_i} = \frac{\partial}{\partial x_j} \left( \left( \mu + \frac{\mu_t}{\sigma_k} \right) \frac{\partial k}{\partial x_j} \right) + \tilde{G}_k - Y_k + S_k \quad (23)$$

$$\frac{\partial(\rho \omega)}{\partial t} + \frac{\partial(\rho \omega u_i)}{\partial x_i} = \frac{\partial}{\partial x_j} \left( \left( \mu + \frac{\mu_t}{\sigma_\omega} \right) \frac{\partial \omega}{\partial x_j} \right) + G_\omega - Y_\omega + D_\omega + S_\omega \quad (24)$$

where  $\tilde{G}_k$ ,  $G_\omega$ ,  $D_\omega$ ,  $Y_k$ , and  $Y_\omega$  are turbulence kinetic energy generation because of the mean velocity gradients, generation of  $\omega$ , the cross-diffusion term, dissipation of  $k$  due to turbulence, and dissipation of  $\omega$  due to turbulence, respectively. Also,  $\sigma_k$  and  $\sigma_\omega$  indicate turbulent Prandtl numbers for  $k$  and  $\omega$ . In  $SSTk - \omega$  turbulence model,  $S_k$  and  $S_\omega$  denote source terms.

### 3.4 Area-weighted average

According to literature, the area-weighted average is used in several research. For instance, Sun et al. [40] applied the area-weighted average for temperature, and Bolduc et al. [40] applied the area-weighted average for two phase flow analysis. Therefore, it has been applied for properties in the outlet of the primary nozzle in this paper. The area-weighted average of a sample quantity of  $X$  is obtained by dividing the summation of the product of the selected field variable and facet area by the total area of the surface as follows [41]:

$$\bar{X} = \frac{1}{A} \int X dA \quad (25)$$

## 4 Result and discussion

In the present study, numerical modeling performs using CFD software for compressible 2D axisymmetric flow. The value of  $1 \times 10^{-6}$  for the relative residual of all dependent

variables considers as the convergence criterion. To validation, the non-equilibrium wet-steam flows have been simulated in the nozzle and ejector.

### 4.1 Nozzle

#### 4.1.1 Independency and validation

Type and number of cells can accelerate convergence and can raise solution accuracy. Therefore, to achieve minimum cell with maximum solution accuracy, mesh independence and choosing the optimum grid are necessary. In this paper, first, the mesh independence is investigated in the Moore B nozzle. The boundary conditions of this nozzle are given in Table 1. Five meshes with  $20 \times 100$ ,  $30 \times 150$ ,  $40 \times 200$ ,  $50 \times 250$ , and  $60 \times 300$  cells, using structured mesh are applied. Figure 2A indicates a clear view of the nozzle mesh domain. Figure 2B shows liquid mass fraction ( $\beta$ ) in nozzle exit for these five meshes. As can be seen,  $\beta$  increases as the number of cells increases. But, these changes become insignificant for mesh with more than  $50 \times 250$  cells. Therefore, this mesh is selected as the optimum grid. The concentration of grids increases in the throat and near walls where the gradients are important.

Wet steam flow is simulated for the Moore B nozzle. Figure 2C shows the comparison of droplet radius ( $r$ ) and static pressure measurement with their values of the experimental test [42, 43]. Acceptable accuracy in results and good agreement with experimental data indicate the appropriated mesh and choosing suitable procedure in problem simulation.

#### 4.1.2 Effect of roughness on flow in the nozzle

Figure 3(A) indicates the nozzle mass flow rate by increasing the surface roughness. Five cases of the average roughness height ( $k_s$ ) have been considered, including;  $0 \mu m$  (smooth),  $30 \mu m$ ,  $100 \mu m$ ,  $300 \mu m$ , and  $1000 \mu m$ . This figure reveals that the growth of roughness height from  $0$  to  $1000 \mu m$  reduces the mass flow rate by 1%.

**Table 1** Boundary conditions of Moore B nozzle

| Moore B Nozzle | Boundary condition<br>[P (kPa), T (K)] | Coordinate<br>[x(m), y(m)]        |
|----------------|--|-----------------------------------|
| Inlet          | [25, 357.6]                            | [-0.25, 0.056]<br>[-0.25, -0.056] |
| Outlet         | [6, 310]                               | [0.5, 0.072]<br>[0.5, -0.072]     |

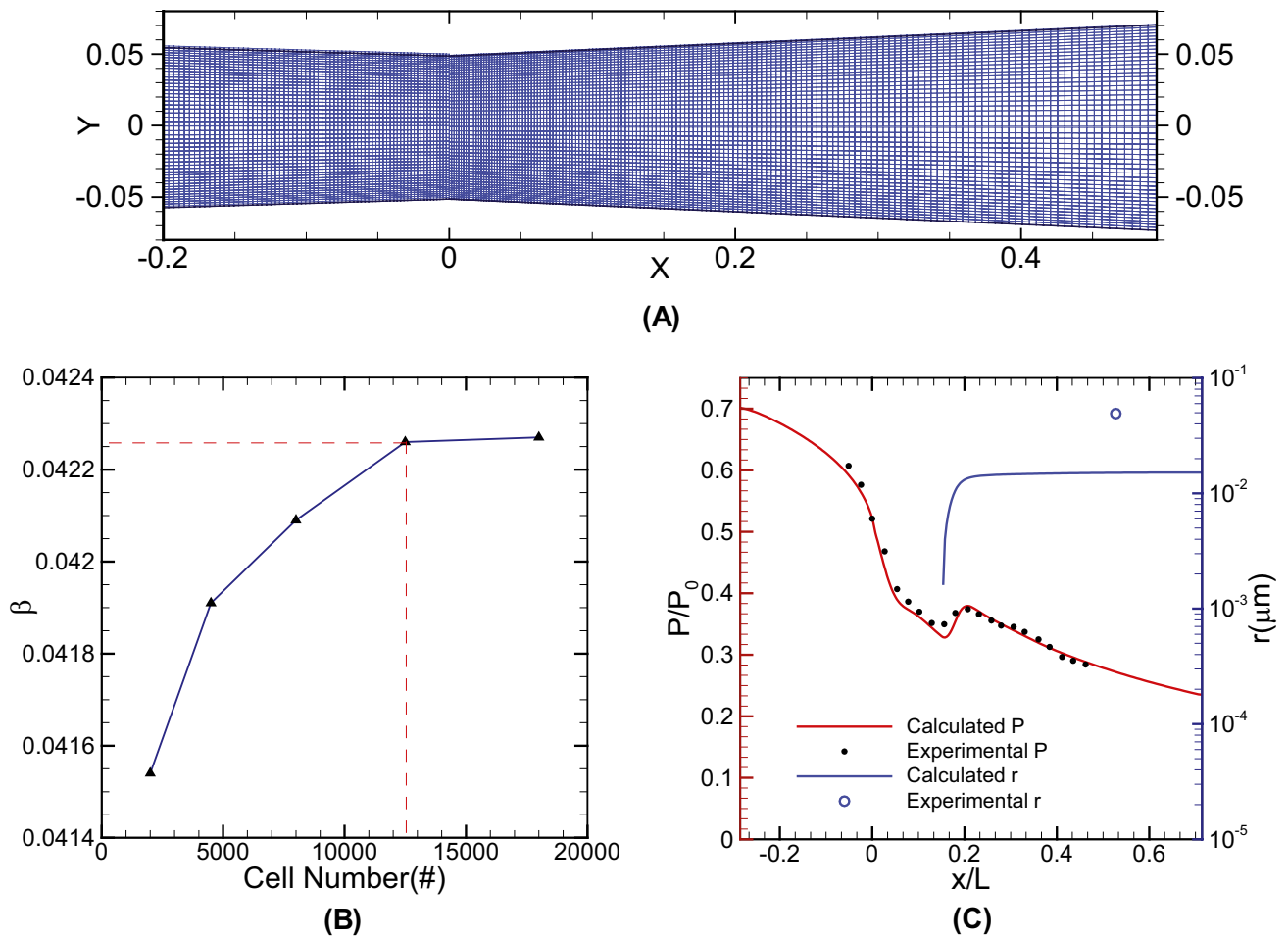
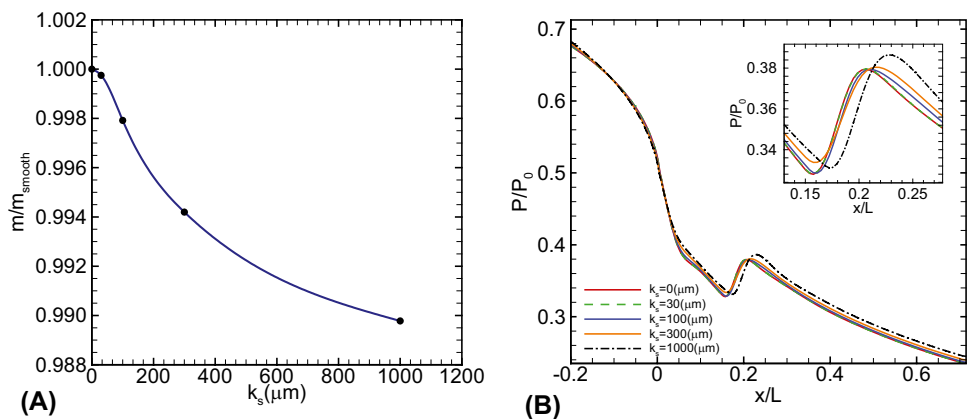


Fig. 2 (A) nozzle geometry and mesh, (B) mesh independence, and (C) solution validation

Figure 3(B) presents the pressure profiles for five different surface roughness values. In all five cases, the inlet and outlet condition maintain at 25 kPa and 6 kPa, respectively. It is found that there is a slight rise in pressure by increasing the roughness. In addition, the roughness delays the condensation shock, and therefore, this shock occurs at a greater distance after the throat.

Fig. 3 Effect of roughness height on (A) mass flow rate and (B) pressure of wet steam nozzle



## 4.2 Ejector

### 4.2.1 Independency and validation

Figure 4A shows the geometry and mesh grid for the proposed ejector to determine the dependence of the results

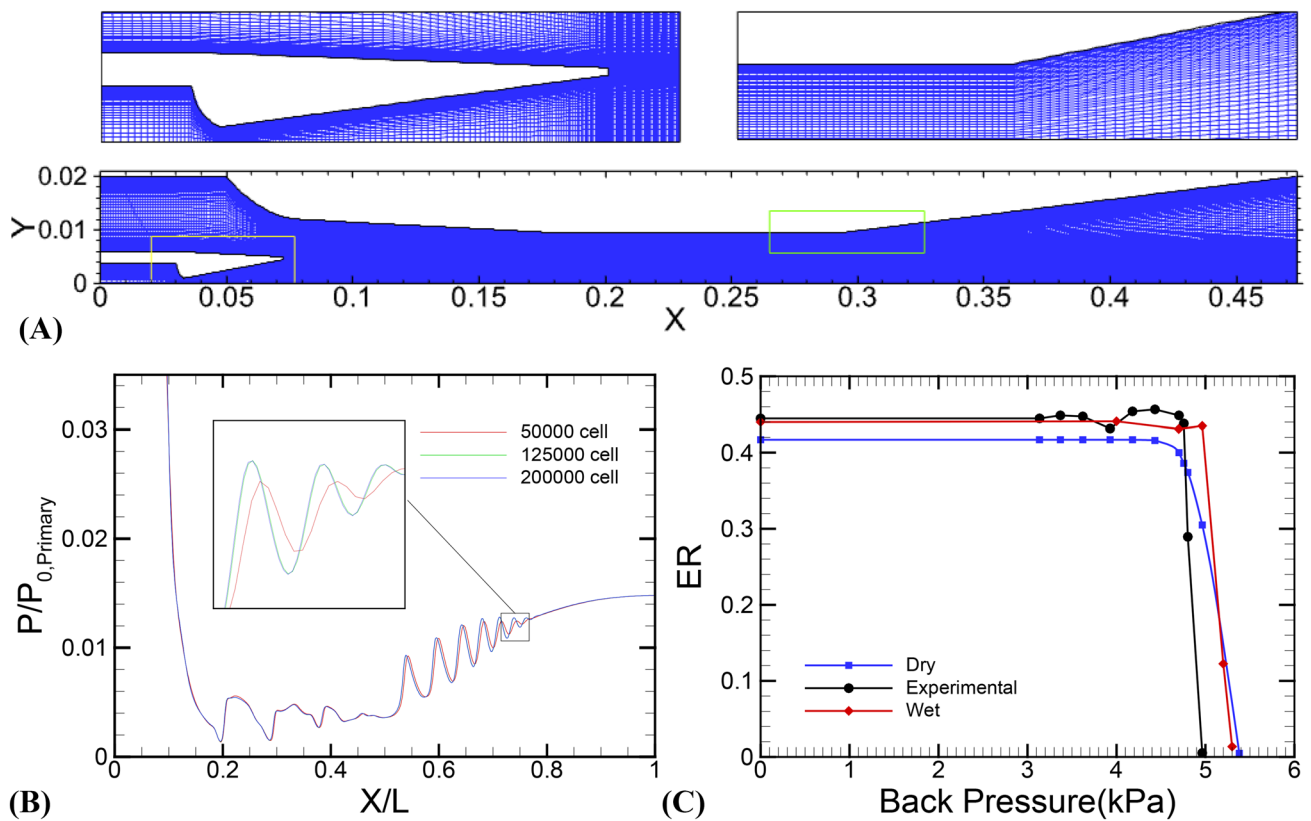


Fig. 4 (A) ejector geometry and mesh (B) mesh independency, and (C) validation

on the mesh density; three different densities of the structural grids, including 50,000, 125,000, and 200,000 cells were applied. The static pressure was selected as parameter of the test of grids. As can be seen in Fig. 4B, there is no significant variation in pressure for mesh with more than 125,000 cells. Therefore, this mesh is chosen as the optimal mesh.

The ER for different backpressure is employed to validate the numerical model. Consider Fig. 4C, which plots ER for wet and dry ejectors in comparison with experimental data [36]. This diagram can give an overview of the ejector performance at different pressure. The results are very similar to the results obtained by the experimental test which can emphasize the validity of the used model.

#### 4.2.2 Effect of the primary nozzle surface roughness on thermodynamic properties

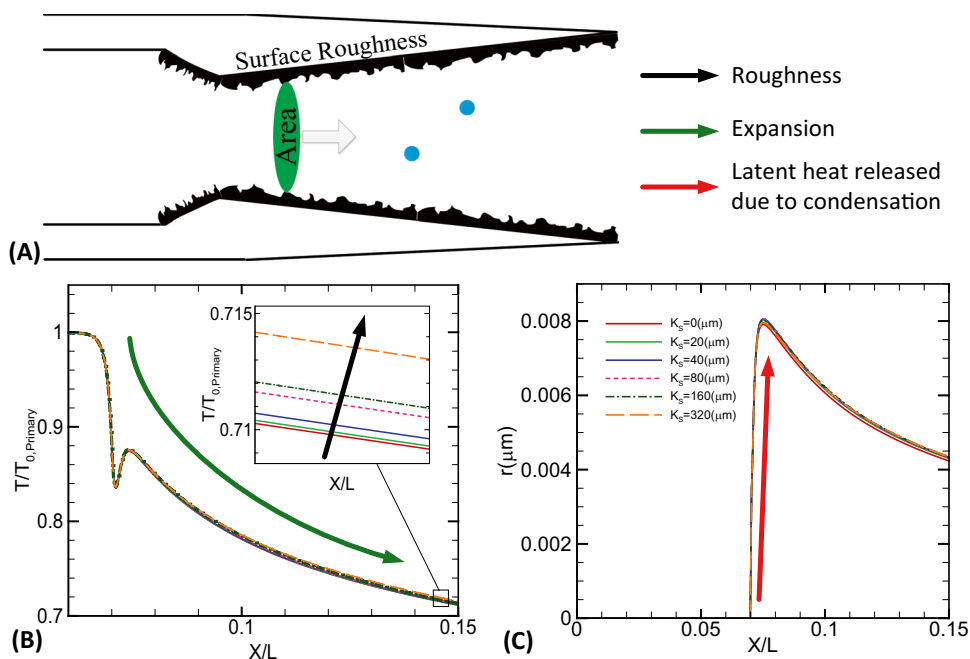
The wet steam ejector is simulated using the CFD model in six different surface roughness heights for the primary nozzle including;  $0\mu\text{m}$  (smooth),  $20\mu\text{m}$ ,  $40\mu\text{m}$ ,  $80\mu\text{m}$ ,  $160\mu\text{m}$ , and  $320\mu\text{m}$ . It should be mentioned that, in this problem, rough surface creates by three reasons, which are: (I) intrinsic surface roughness, (II) machining process, and (III)

corrosion and erosion due to high-velocity flow and collision of condensed droplets with the nozzle wall. To show the effects of the primary nozzle surface roughness, six properties of wet steam are selected due to their importance in numerical studies, including pressure, temperature, Mach number, average droplet radius ( $r$ ), droplet growth rate ( $\dot{r}$ ), and liquid mass fraction ( $\beta$ ).

Investigating compressible flow in the supersonic adiabatic nozzle shows that three main factors affect the flow including; cross-section area changes, heat transfer due to non-equilibrium condensation, and roughness (see Fig. 5A). It should be noted that simultaneous examination of these factors complicates the issue due to the complex relationships between properties, however; they can be examined separately.

The first important factor in supersonic flow is the area change in the primary nozzle which means an increase in diameter of the nozzle exit cross section, resulting in steam expansion. Change of this parameter can vary the secondary mass flow rate in the ejector. It can be seen that the high expansion rate along the primary nozzle occurs due to an increase in the cross-section area (Fig. 5B). This is completely in agreement with the dynamic behavior of compressible adiabatic vapor through a diffuser when the flow

**Fig. 5** Effective parameters in the primary nozzle; (A) schematic of the primary nozzle, (B) temperature ratio of the centerline, and (C) average droplet radius



is supersonic [43]. Steam is dry saturated at the inlet of the nozzle and expands up to Wilson line where the maximum supercooling occurs. At this point, nucleation occurs and temperature and pressure jump due to latent heat transfer from water droplet to steam. Next, steam expansion continues up to the nozzle outlet. It can be clearly seen in Fig. 5B that the maximum variation in temperature is due to expansion in the primary nozzle compared to latent heat and friction effects.

Latent heat transfer due to non-equilibrium condensation is the second factor which is the predominant phenomenon at  $\frac{x}{L} = 0.07$  to  $\frac{x}{L} = 0.08$  in the primary nozzle (see Fig. 5C). This position can be distinguished as a sudden jump in average droplet radius. An increment in droplets radius means more latent heat transition to the steam phase which causes a rise of the static temperature, returning flow to the thermodynamic equilibrium conditions and reducing nucleation rate and steam subcooling levels.

To better understand the effect of roughness on flow as the third factor, the area-weighted average values of mentioned properties are calculated at the primary nozzle exit (PNE), mixing chamber exit (MCE), and constant area exit (CAE). These values are plotted in Fig. 6. According to the Fanno Flow, the presence of friction in supersonic flow increases both pressure and temperature [44]. This can be seen in Fig. 6(A) where the pressure rises from 2100 Pa for smooth wall to 2500 Pa for 320  $\mu\text{m}$  roughness height. The curve shows that the temperature rising is intensified by increasing surface roughness, while pressure increase moderately. Furthermore, average droplet radius, droplet growth rate, and liquid mass fraction reduce due to temperature

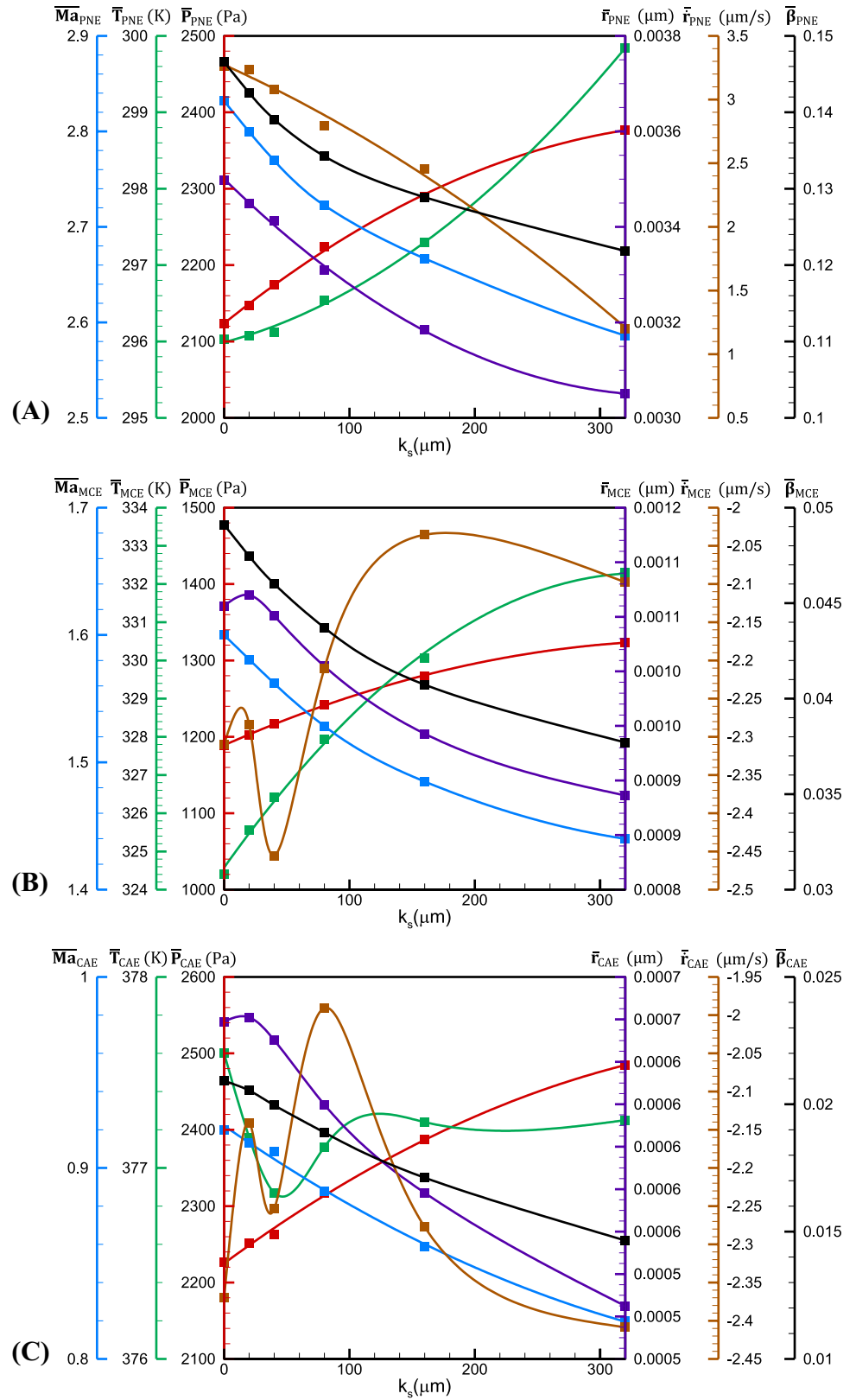
increment. Although these variations seem to be slight, they strongly affect flow condition ahead of shock chain and consequently ER of the ejector (see Fig. 7). Figure 6(B) and (C) indicate similar properties for MCE and CAE. The fluctuating parameters in these figures show the displacement of maximum and minimum points in the shock chain. An interesting point in Fig. 6(B) and (C) is the negative values for droplet growth rate, which is demonstrated the evaporation of droplets in the mixing chamber and constant area. Comparison of Mach number in Fig. 6 demonstrates that mentioned property reduces more than 40% in each section from PNE to MCE and further CAE.

As can be seen in Fig. 7(A), steam expansion continues in the mixing chamber and its pressure ratio drops to 0.2 which means that the mixing pressure is less than secondary flow pressure. From this point to the outlet of the ejector, the flow is compressed, and a series of oblique aerodynamic shocks is formed. However, the pressure rising becomes smoother in the constant area section, between  $\frac{x}{L} = 0.42$  to  $\frac{x}{L} = 0.56$ . Figure 7(A) highlights that the pressure pattern is similar for different roughness. But it causes variation as follows:

- The aerodynamic shocks move upstream.
- Aerodynamic shock strength decreases at the beginning of the diffuser.
- The level of static pressure has increased along the centerline.

The pressure diagram clearly shows these changes, especially between  $\frac{x}{L} = 0.26$  to  $\frac{x}{L} = 0.34$ , where the local valley has completely changed. Further, these changes can be seen

**Fig. 6** Average value of flow properties at (A) the primary nozzle exit (PNE) (B) the mixing chamber exit (MCE) (C) the constant area exit (CAE)



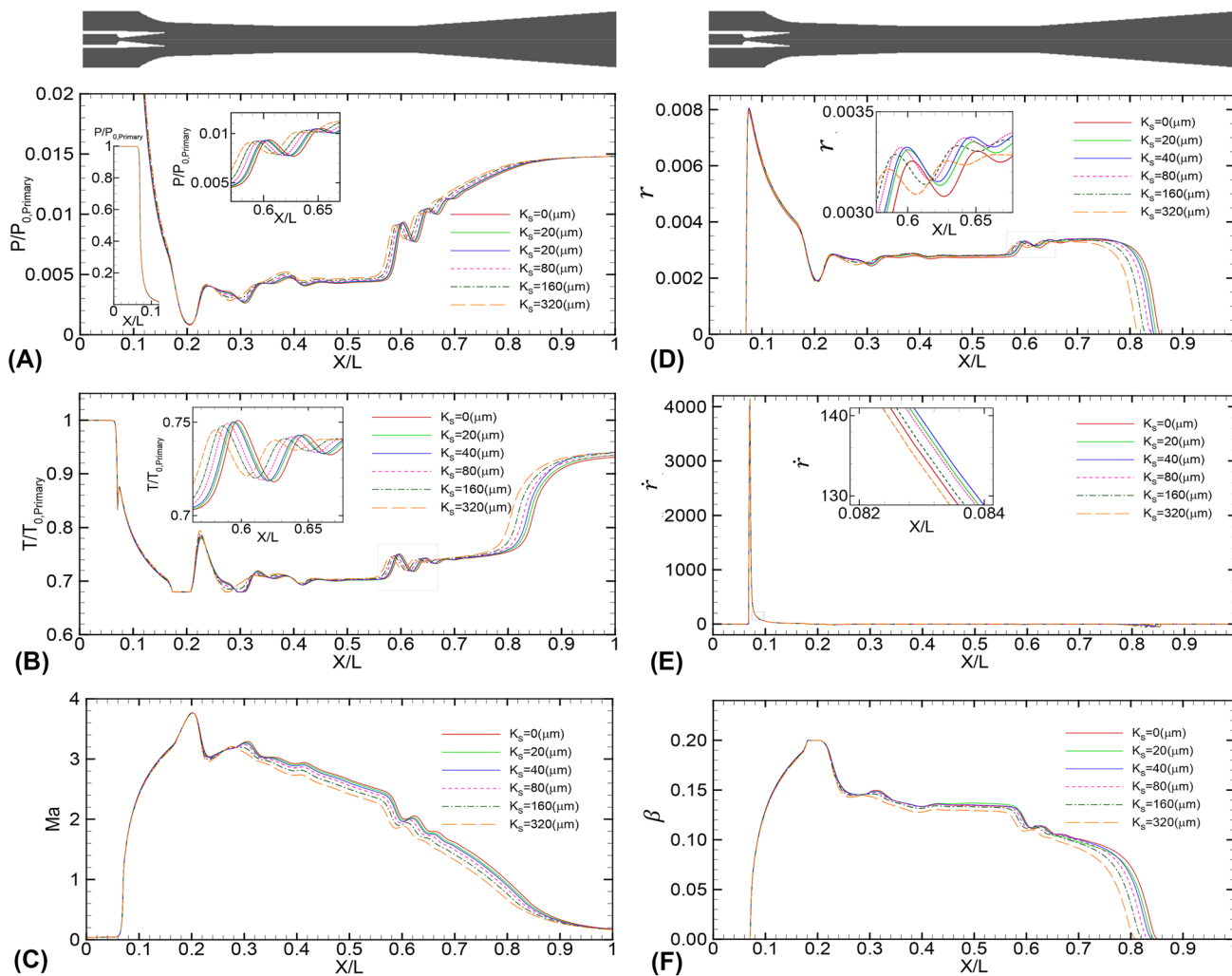


**Fig. 7** Distribution of different parameters on the centerline of the ejector by the increment of roughness in the primary nozzle (A) pressure, (B) temperature, (C) Mach number, (D) average droplet radius, (E) droplet growth rate, and (F) liquid mass fraction

in  $T/T_{0,Primary}$  in Fig. 7(B). Temperature distribution along with the ejector for different wall roughness is shown in Fig. 7(B). Temperature curves generally have a downward, fluctuating, and upward pattern, respectively. Similar to the pressure diagram, it can be seen the temperature fluctuates due to the presence of the shock chain. Figure 7(B) indicates that the crest-trough interval of temperature fluctuation decreases at the end of the constant area section. However, the temperature increases along with the diffuser.

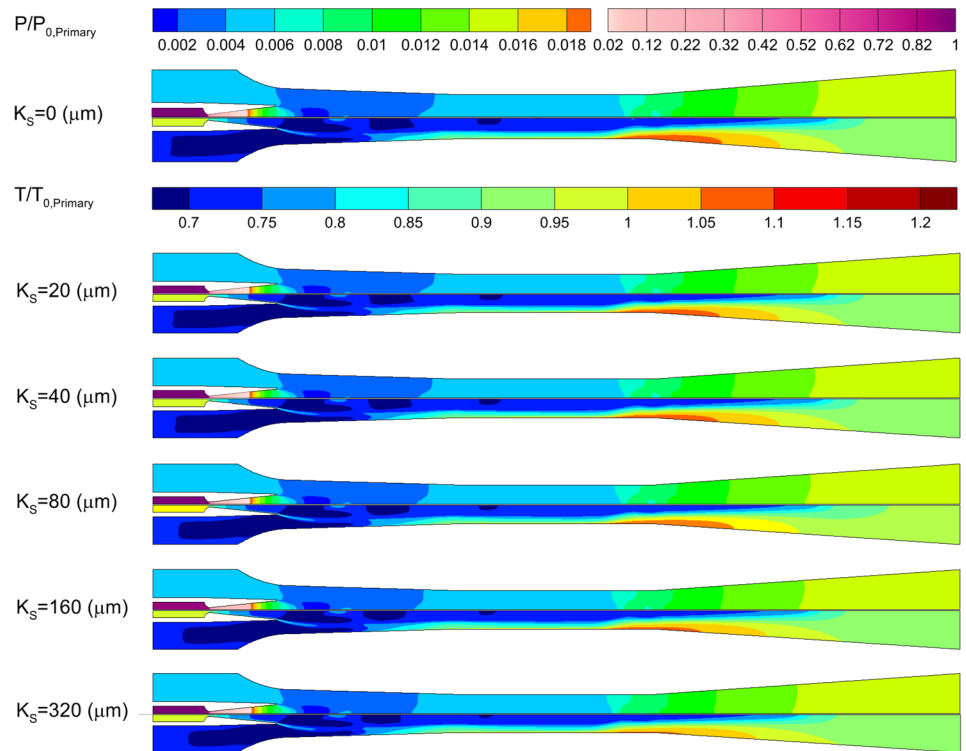
To indicate the pressure and temperature distribution of the whole flow field, their contour has been brought in Fig. 8. These contours show that the effect of shock is reduced at the near-wall zone. It is also well observed that the lowest pressure occurs at the mixing chamber, which results in better suction of the secondary stream into the ejector. This figure clearly shows the pressure rising in the constant area section. Furthermore, temperature contour shows that for smooth surface in the primary nozzle, a high-temperature

zone emerges near the wall at the beginning of the diffuser. This value decrease by the increment of roughness. Therefore, the temperature difference between the centerline and wall of the diffuser declines by increasing roughness.

Figure 7(C) shows the sensitivity of the Mach number at the centerline. It is apparent that an abrupt increase in Mach number begins from the primary nozzle and reaches up to 1 at the nozzle throat. The continuous expansion causes the Mach number to increase until the shock chain occurs. Steam compression from the mixing chamber to the end of the ejector reduces Mach number. However, it fluctuates in some points. It is evident that the major effect of the pressure increase is to reduce the values of Mach number between  $\frac{x}{L} = 0.3$  to  $\frac{x}{L} = 0.9$ . Figure 9 provides a better vision of the distribution of Mach number throughout the ejector and clearly shows shock chain attenuation and displacement.

As can be seen in downside of Fig. 9, the diamond pattern of the shock chain extended to the mixing chamber and

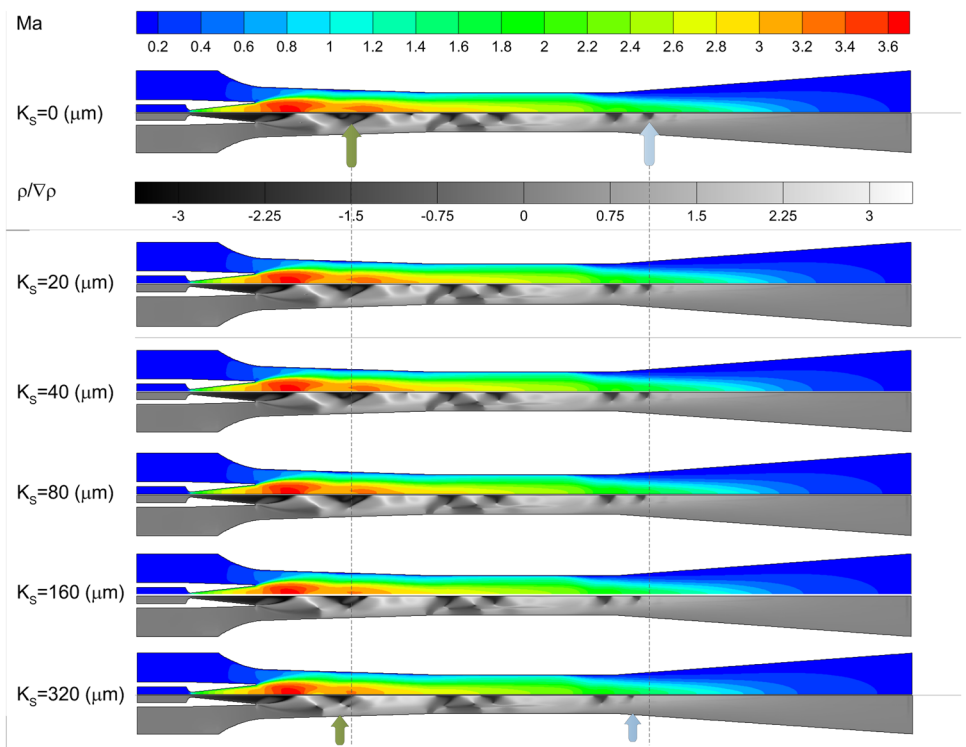
**Fig. 8** Contour of pressure (up) and temperature (down)



constant area walls. The shock wave then strikes the constant area wall and reflects from the wall generating a new shock. This image can provide valuable diagnostic information about non-uniformities in flow and location, strength,

and displacement of the shock wave. Roughness impacts on shock chain so that, as the roughness increases, the shock chain moves upstream and decreases in strength. This phenomenon has been shown by dashline. This figure easily

**Fig. 9** Contour of Mach number (up) and density/density gradient (down)



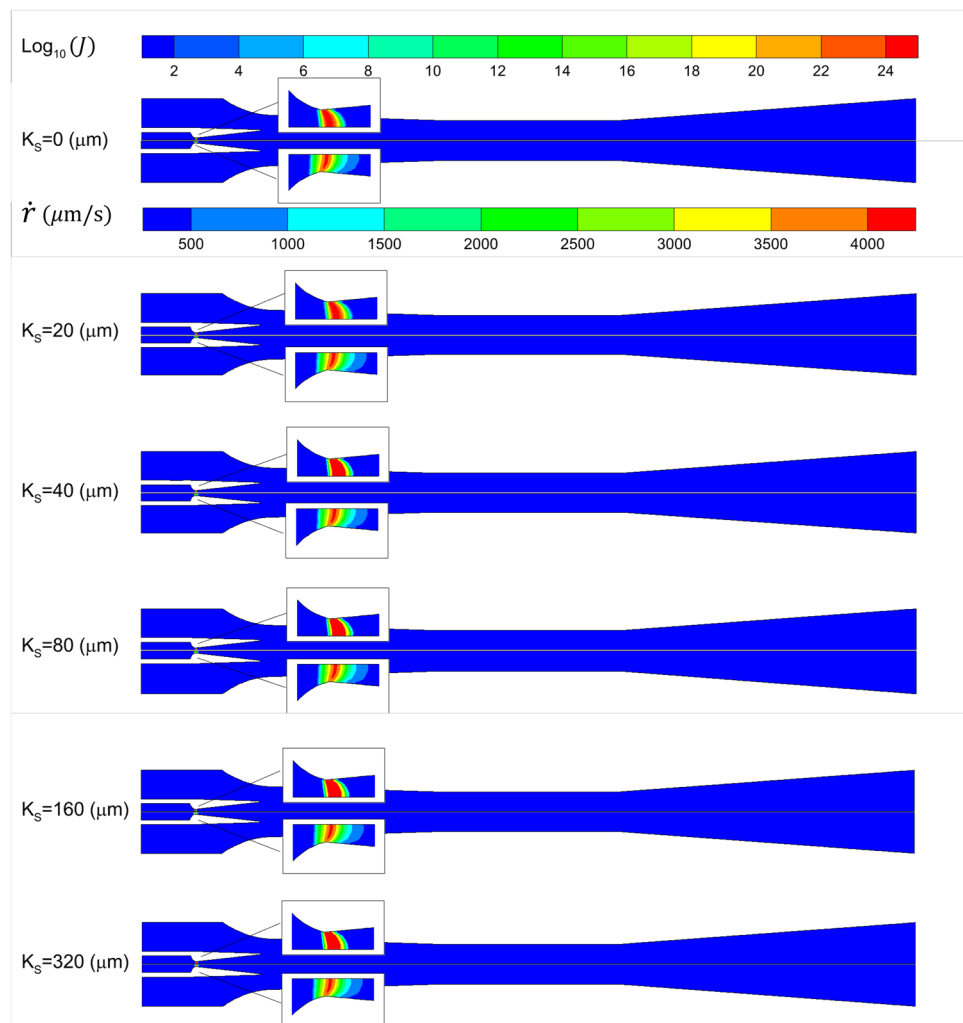
indicates the density gradient due to condensation shock in the primary nozzle throat. Furthermore, the interaction of primary and secondary flow can be seen in the form of a thin strip of dark gray in the mixing chamber.

Figure 7(D) to (F) show the thermodynamic properties diagram. As can be seen, these properties severely increase around  $\frac{x}{L} = 0.07$ , where the nucleation occurs. At this point, the condensed nuclei are attached and form droplets. As the nucleation rate reaches the maximum value, more nuclei join each other, and the droplet radius rapidly increases. Transmitted latent heat from droplets to steam phase increases flow pressure and consequently limits droplet growth rate (Fig. 7(E)). Thereby, the droplet radius decreases. The behavior of wet steam parameters is in contrast with the pressure and temperature trend. In other words, the higher static temperature and pressure result in a lower average droplet radius and liquid mass fraction. With increasing surface roughness, the liquid mass fraction emerging zone is significantly reduced. There is a similar trend for average droplet radius, which is in good agreement with the

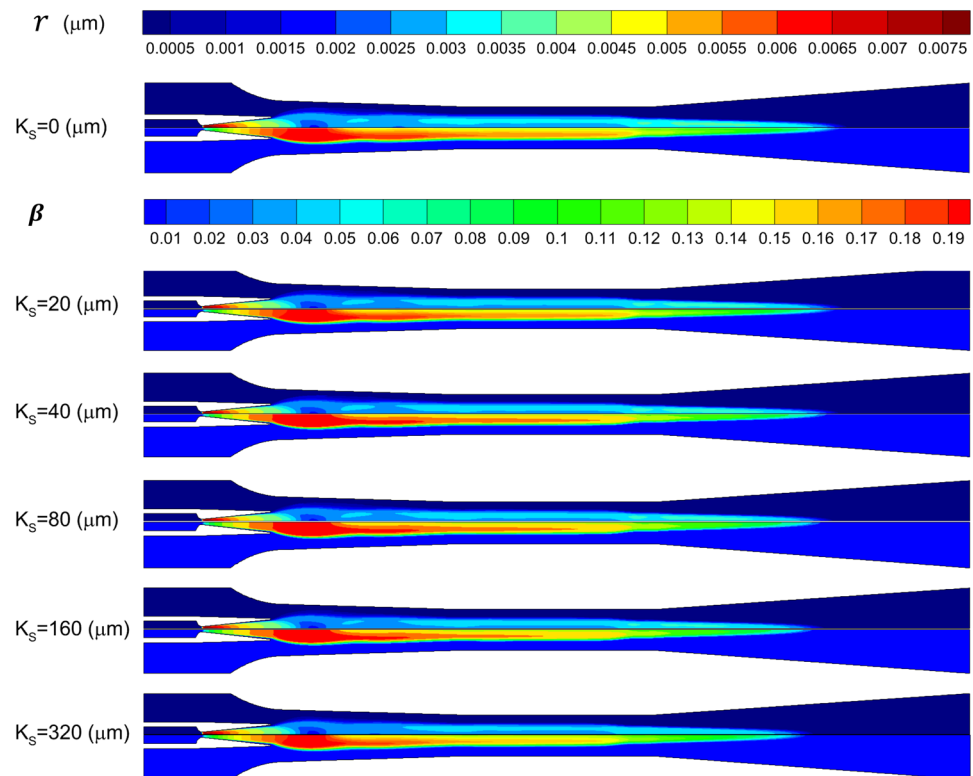
temperature increase in the diffuser. Furthermore, the thermodynamic properties contours corresponding to different primary nozzle roughness are demonstrated in Figs. 10 and 11. Figure 10 indicates the only point in the ejector where the nucleation and consequently droplet growth rate appears. According to the simulation result in Fig. 11, the near-wall zone of the mixing chamber, constant area and diffuser have the minimum value for average droplet radius and liquid mass fraction. As seen in the temperature contour, the temperature rises from the center of the ejector to the walls and reaches its maximum at the side of the ejector wall. It seems that this increase in temperature is the main factor in reducing the liquid mass fraction and the average droplet radius.

Figure 12 has been plotted to evaluate the influence of surface roughness on ER and COP of the ejector. It illustrates the growth of the surface roughness in the range of 0 to  $320\mu\text{m}$  results in reduction of ER and COP of the refrigeration cycle by 3.67% and 3.8%, respectively. This is because of more energy losses by the increment of surface roughness. Roughness height of  $20\mu\text{m}$  seems to

**Fig. 10** Contour of droplet nucleation rate (up) and droplet growth rate (down)



**Fig. 11** Contour of average droplet radius (up) and liquid mass fraction (down)



be a critical point where the effect of wall roughness less than  $20\mu\text{m}$  on ER can be neglected and ER drops down extremely for roughness more than  $20\mu\text{m}$ . Comparing Fig. 12 with Fig. 4C reveals that ER has a similar trend by increasing backpressure and roughness. In fact, both of them lead to more loss of energy.

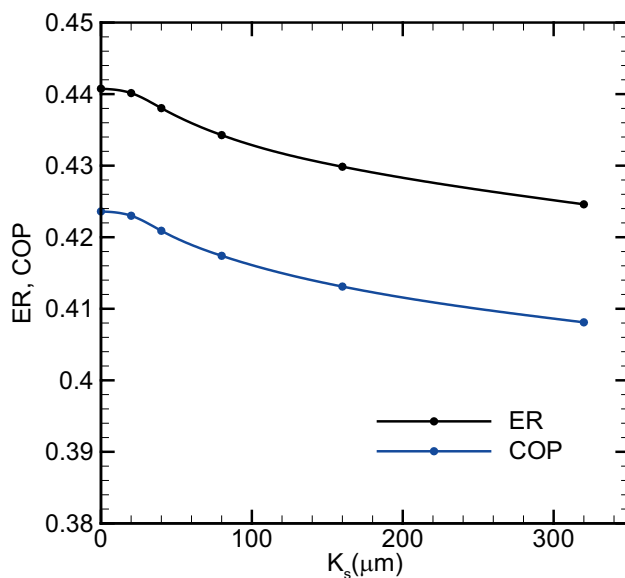


**Fig. 12** Effect of roughness height on ER and COP of refrigeration cycle

## 5 Conclusion

The effect of the primary nozzle surface roughness on the performance of wet steam ejectors with water as a working flow is analyzed. The practical aim of the present work is to understand better the correlation of thermodynamic properties with change in the surface roughness for possible promotion in the design and operation of wet steam ejectors. The most remarkable results from this study are as follows:

- The pressure and temperature increase due to roughness of the primary nozzle.
- Mach number, average droplet radius, droplet growth rate, and liquid mass fraction have a reduction trend because of roughness of the primary nozzle.
- Wall roughness influences the passing flow through the ejector, wherein roughness affects flow condition ahead of the primary nozzle and causes the section in which aerodynamic shock takes place to move upstream.
- Aerodynamic shock strength decreases at the beginning of the diffuser by increasing the wall roughness in the primary nozzle.
- Increment of primary nozzle surface roughness from 0 to  $320\mu\text{m}$  decreases ER and COP of the refrigeration cycle by 3.67% and 3.8%, respectively.

Therefore, designers and operators should be considered the roughness effects in the design and operation of wet

steam ejectors. Furthermore, the inner surface of the ejector should be monitored and controlled regularly. As future work, it is proposed to extend the studies in the field of effect of surface roughness on wet steam ejectors with water as working fluid which can open new research field about wet flow, surface roughness, and corrosion/erosion in equipment. The authors hope to address this field by providing an experimental setup or collaborating with other researchers.

## References

- Edathol J, Brezgin D, Aronson K, Kim HD (2020) Prediction of non-equilibrium homogeneous condensation in supersonic nozzle flows using Eulerian-Eulerian models. *Int J Heat Mass Transf* 1(152):119451. <https://doi.org/10.1016/j.ijheatmasstransfer.2020.119451>
- Yazdani S, Lakzian E (2020) Numerical simulation and passive control of condensing flow through turbine blade by NVD Method Using Eulerian-Lagrangian Model. *Comput Math Appl* 80(1):140–160. <https://doi.org/10.1016/j.camwa.2020.03.007>
- Ding H, Tian Y, Wen C, Wang C, Sun C (2021) Polydispersed droplet spectrum and exergy analysis in wet steam flows using method of moments. *Appl Therm Eng* 182:116148. <https://doi.org/10.1016/j.applthermaleng.2020.116148>
- Dykas S, Wróblewski W (2011) Single-and two-fluid models for steam condensing flow modeling. *Int J Multiph Flow* 37(9):1245–1253. <https://doi.org/10.1016/j.ijmultiphaseflow.2011.05.008>
- Alekseev RA, Gribin VG, Tishchenko AA, Gavrillov IY, Tishchenko VA, Popov VV (2018) Application of PTV method for investigation of polydisperse wet steam flow. In *J Phys: Confer Series* 1128(1):012093. IOP Publishing. <https://doi.org/10.1088/1742-6596/1128/1/012093>
- Kafaei A, Salmani F, Lakzian E, Wróblewski W, Vlaskin MS, Deng Q (2022) The best angle of hot steam injection holes in the 3D steam turbine blade cascade. *Int J Therm Sci* 1(173):107387. <https://doi.org/10.1016/j.ijthermalsci.2021.107387>
- Milazzo A, Rocchetti A (2015) Modelling of ejector chillers with steam and other working fluids. *Int J Refrig* 1(57):277–287. <https://doi.org/10.1016/j.ijrefrig.2015.05.015>
- Besagni G, Cristiani N, Croci L, Guédon GR, Inzoli F (2021) Multi-scale evaluation of ejector performances: The influence of refrigerants and ejector design. *Appl Therm Eng* 5(186):116502. <https://doi.org/10.1016/j.applthermaleng.2020.116502>
- Pérez BP, Carrillo JA, de La Flor FJ, Lissén JM, Navarro AM (2021) Thermo-economic analysis of CO<sub>2</sub> Ejector-Expansion Refrigeration Cycle (EERC) for low-temperature refrigeration in warm climates. *Appl Therm Eng* 1(188):116613. <https://doi.org/10.1016/j.applthermaleng.2021.116613>
- Sharifi N, Boroomand M, Sharifi M (2013) Numerical assessment of steam nucleation on thermodynamic performance of steam ejectors. *Appl Therm Eng* 52(2):449–59. <https://doi.org/10.1016/j.applthermaleng.2012.12.003>
- Aliabadi MA, Bahiraei M (2021) Effect of water nano-droplet injection on steam ejector performance based on non-equilibrium spontaneous condensation: A droplet number study. *Appl Therm Eng* 5(184):116236. <https://doi.org/10.1016/j.applthermaleng.2020.116236>
- Li A, Yuen AC, Chen TB, Wang C, Liu H, Cao R, Yang W, Yeoh GH, Timchenko V (2019) Computational study of wet steam flow to optimize steam ejector efficiency for potential fire suppression application. *Appl Sci* 9(7):1486. <https://doi.org/10.3390/app9071486>
- Zhang G, Dykas S, Li P, Li H, Wang J (2020) Accurate condensing steam flow modeling in the ejector of the solar-driven refrigeration system. *Energy* 1(212):118690. <https://doi.org/10.1016/j.energy.2020.118690>
- Wang C, Wang L, Zhao H, Du Z, Ding Z (2016) Effects of superheated steam on non-equilibrium condensation in ejector primary nozzle. *Int J Refrig* 1(67):214–226. <https://doi.org/10.1016/j.ijrefrig.2016.02.022>
- Wang X, Dong J, Li A, Lei H, Tu J (2014) Numerical study of primary steam superheating effects on steam ejector flow and its pumping performance. *Energy* 15(78):205–211. <https://doi.org/10.1016/j.energy.2014.10.004>
- Yang Y, Karvounis N, Walther JH, Ding H, Wen C (2021) Effect of area ratio of the primary nozzle on steam ejector performance considering nonequilibrium condensations. *Energy* 15(237):121483. <https://doi.org/10.1016/j.energy.2021.121483>
- Ariafar K, Buttsworth D, Al-Doori G, Sharifi N (2016) Mixing layer effects on the entrainment ratio in steam ejectors through ideal gas computational simulations. *Energy*. 95:380–92. <https://doi.org/10.1016/j.energy.2015.12.027>
- Tang Y, Liu Z, Li Y, Wu H, Zhang X, Yang N (2019) Visualization experimental study of the condensing flow regime in the transonic mixing process of desalination-oriented steam ejector. *Energy Convers Manage* 1(197):111849. <https://doi.org/10.1016/j.enconman.2019.111849>
- Zou JJ, Zhou J, Lu HQ, Hu Y (2012) Experimental investigation on starting process of supersonic single-stage air ejector. *J Therm Sci* 21(4):348–353. <https://doi.org/10.1007/s11630-012-0554-1>
- Foroozesh F, Khoshnevis AB, Lakzian E (2020) Improvement of the wet steam ejector performance in a refrigeration cycle via changing the ejector geometry by a novel EEC (Entropy generation, Entrainment ratio, and Coefficient of performance) method. *Int J Refrig* 1(110):248–261. <https://doi.org/10.1016/j.ijrefrig.2019.11.006>
- Foroozesh F, Khoshnevis AB, Lakzian E (2020) Investigation on the effects of water steam ejector geometry in the refrigeration systems using entropy generation assessment. *J Therm Anal Calorim* 141(4):1399–1411. <https://doi.org/10.1007/s10973-019-09128-1>
- Lakzian E, Hajian M, Farahmand A (2018) The entropy generation rate minimization for a proposed air ejector for the carpet industry. *Meccanica* 53(1):145–159. <https://doi.org/10.1007/s11012-017-0706-1>
- Dong J, Hu Q, Yu M, Han Z, Cui W, Liang D, Ma H, Pan X (2020) Numerical investigation on the influence of mixing chamber length on steam ejector performance. *Appl Therm Eng* 25(174):115204. <https://doi.org/10.1016/j.applthermaleng.2020.115204>
- Zhang G, Dykas S, Yang S, Zhang X, Li H, Wang J (2020) Optimization of the primary nozzle based on a modified condensation model in a steam ejector. *Appl Therm Eng* 5(171):115090. <https://doi.org/10.1016/j.applthermaleng.2020.115090>
- Zhang G, Wang X, Pourranjbar D, Dykas S, Li H, Chen J (2022) The comprehensive analysis of the relationship between the latent heat, entrainment ratio, and ejector performance under different superheating degree conditions considering the non-equilibrium condensation. *Appl Therm Eng* 5(200):117701. <https://doi.org/10.1016/j.applthermaleng.2021.117701>
- Wang C, Wang L, Zou T, Zhang H (2017) Influences of area ratio and surface roughness on homogeneous condensation in ejector primary nozzle. *Energy Convers Manage* 149:168–74. <https://doi.org/10.1016/j.enconman.2017.07.025>
- Mahmoudian J, Mazzelli F, Milazzo A, Rocchetti A (2020) Experimental and numerical activity on a prototype ejector chiller. In *J Phys: Confer Series* 1599(1):012056. IOP Publishing. <https://doi.org/10.1088/1742-6596/1599/1/012056>
- Zhang H, Wang L, Jia L, Wang X (2018) Assessment and prediction of component efficiencies in supersonic ejector with friction

- losses. *Appl Therm Eng* 25(129):618–627. <https://doi.org/10.1016/j.applthermaleng.2017.10.054>
29. Zhang H, Wang L, Jia L, Zhao H, Wang C (2018) Influence investigation of friction on supersonic ejector performance. *Int J Refrig* 1(85):229–239. <https://doi.org/10.1016/j.ijrefrig.2017.09.028>
  30. Wang L, Yan J, Wang C, Li X (2017) Numerical study on optimization of ejector primary nozzle geometries. *Internatl J Refrige* 76:219–29. <https://doi.org/10.1016/j.ijrefrig.2017.02.010>
  31. Brezgin DV, Aronson KE, Mazzelli F, Milazzo A (2017) The surface roughness effect on the performance of supersonic ejectors. *Thermophys Aeromech* 24(4):553–61. <https://doi.org/10.1134/S0869864317040060>
  32. Pillai A, Prasad BV (2018) Effect of wall surface roughness on condensation shock. *Int J Therm Sci* 1(132):435–445. <https://doi.org/10.1016/j.ijthermalsci.-2018.06.028>
  33. Han X, Liu X, Yuan Y, Han Z (2019) Effect of blade surface roughness on condensation process in a stator cascade. *Int J Numer Meth Heat Fluid Flow*. <https://doi.org/10.1108/HFF-10-2019-0736>
  34. Ding H, Li Y, Lakzian E, Wen C, Wang C (2019) Entropy generation and exergy destruction in condensing steam flow through turbine blade with surface roughness. *Energy Convers Manage* 15(196):1089–1104. <https://doi.org/10.1016/j.enconman.2019.06.066>
  35. Esfe HB, Kermani MJ, Avval MS (2015) Effects of surface roughness on deviation angle and performance losses in wet steam turbines. *Appl Therm Eng* 5(90):158–173. <https://doi.org/10.1016/j.applthermaleng.2015.07.007>
  36. Ruangtrakoon N, Aphornratana S, Sriveerakul T (2011) Experimental studies of a steam jet refrigeration cycle: effect of the primary nozzle geometries to system performance. *Exp Thermal Fluid Sci* 35(4):676–683. <https://doi.org/10.1016/j.expthermflusci.-2011.01.001>
  37. Ebrahimi-Fizik A, Lakzian E, Hashemian A (2020) Numerical investigation of wet inflow in steam turbine cascades using NURBS-based mesh generation method. *Int Commun Heat Mass Transfer* 1(118):104812. <https://doi.org/10.1016/j.icheatmasstransfer.-2020.104812>
  38. Mazzelli F, Little AB, Garimella S, Bartosiewicz Y (2015) Computational and experimental analysis of supersonic air ejector: Turbulence modeling and assessment of 3D effects. *Int J Heat Fluid Flow* 1(56):305–316. <https://doi.org/10.1016/j.ijheatfluidflow.-2015.08.003>
  39. Cebeci T, Chang KC (1978) Calculation of incompressible rough-wall boundary-layer flows. *AIAA J* 16(7):730–735. <https://doi.org/10.2514/3.7571>
  40. Bolduc CP, Van Dam N (2021) Development of a four-fluid model for condensing steam flows. *Ann Nucl Energy* 1(151):107893. <https://doi.org/10.1016/j.anucene.2020.-107893>
  41. Federico M, Francesco G, Adriano M (2017) CFD modelling of the condensation inside a Supersonic Nozzle: implementing customized wet-steam model in commercial codes. *Energy Procedia* 1(126):34–41. <https://doi.org/10.1016/j.egypro.2017.08.053>
  42. Senguttuvan S, Lee JC (2019) Numerical study of wet-steam flow in Moore nozzles. *J Mech Sci Technol* 33(10):4823–4830. <https://doi.org/10.1007/s12206-019-0923-8>
  43. Kermani MJ, Gerber AG (2003) A general formula for the evaluation of thermodynamic and aerodynamic losses in nucleating steam flow. *Int J Heat Mass Transf* 46(17):3265–3278. [https://doi.org/10.1016/S0017-9310\(03\)00096-6](https://doi.org/10.1016/S0017-9310(03)00096-6)
  44. White FM (2016) *Fluid Mechanics 8th Edition*, McGraw-Hill Education

**Publisher's Note** Springer Nature remains neutral with regard to jurisdictional claims in published maps and institutional affiliations.